

Domain formation in the deposition of thin films of two-component mixtures

Tung B. T. To, Fábio D. A. Aarão Reis

*Instituto de Física, Universidade Federal Fluminense,
Avenida Litorânea s/n, 24210-340 Niterói, RJ, Brazil*

Abstract

We perform a kinetic Monte Carlo simulation study of a model of thin film deposition of a two-component mixture in which the activation energy for diffusion of an adatom is additive over its nearest neighbors and in which the interactions between adatoms of the same species are stronger than those between adatoms of different species. The film morphology is investigated for broad ranges of values of the ratios between terrace diffusivity and atomic flux, of the probabilities of detachment from lateral neighbors, and of probabilities of crossing terrace edges. First, we consider a symmetric case in which the interactions of adatoms of the same species are the same for the two components. For low and intermediate temperatures, we show the formation of narrow domains, whose widths are 3-30 lattice constants, which meander in the layers parallel to the substrate, and are connected through very long distances. The domain width depends on the diffusivity-flux ratio of the same species, but it is weakly affected by interactions of different species, so rough estimates of that width can be obtained by using tabulated properties of films with a single component. At high temperatures, the separation of domains is enhanced, but their long distance connectivity is lost, which shows that the formation of the long meandering domains is restricted to a certain range of temperature and flux. Similar morphological features are obtained when the intra-species interactions are different and the adatom diffusion coefficients on terraces of the same species differ up to two orders of magnitude. An approximate scaling relation for the domain width is ob-

Email addresses: tungto@if.uff.br (Tung B. T. To), reis@if.uff.br (Fábio D. A. Aarão Reis)

tained, but the species with the largest mobility constrains the temperature range in which the long connected domains are found.

Keywords:

thin films, computer simulations, domain structure, nanostructured materials, connectivity

1. Introduction

The separation of domains in thin films with different components such as metals, semiconductors, or organic molecules is important for their technological applications because the domain organization may provide special mechanical, chemical, optical, or electronic properties to the films and may be used to design nanostructures with particular shapes. For instance, phase separation is helpful for production of nanowires after selective removal of one of the components of binary alloy films [2, 20, 49] and domain formation is required for photovoltaic applications of hybrid organic films [5, 34].

The production of films with the desired morphologies at microscale or nanoscale is known to depend on the thorough control of the deposition conditions, which motivated several models of deposition of binary alloy films in the last decades. In one of the pioneering models, the growth of Al-Ge films was represented by the sequential addition of a small number of layers followed by the relaxation according to an Ising Hamiltonian [2]. These features are experimentally observed in mixtures of metallic [1, 20] and semiconductor [30] components. The possibility of lateral and vertical modulation of concentration, which depends on the growth conditions, was shown in a phase-field model in Ref. [36]. This type of model also describes the deposition of films at a coarse-grained level, with applications to mixtures of Cu and Mo [3] and of C and Ni [27, 28]. There are also several models describing the atomic scale processes in the deposition of alloy films [11, 33, 24], in many cases including applications to specific materials such as Ge-Mn [42], Ni-Ti [52], Ga-As-Bi [44], CoPt/SiO₂ [35], PbTe-CdTe [40, 41], Ni-SrTiO₃ [25], and Si-Al [49], Ag-Cu [16], and Ag-Au [17]. In models with relaxation processes restricted to the film surface, an important result is the description of compositional modulations in the vertical and/or in the lateral directions at nanoscale, as observed in experiments [42, 52, 50, 40, 41, 25, 49, 28, 47].

The atomistic models for deposition of films with binary mixtures represent the competition of atomic/molecular flux and the diffusion of the ad-

sorbed atoms/molecules. They extend the framework previously developed for modeling thin film deposition with a single chemical species [39, 18]. One of the most successful models for metal and semiconductor epitaxy is that of Clarke and Vvedensky (CV) [7], in which the rate of adatom hops depends on an energy barrier that characterizes the current site neighborhood; for details, see e.g. Ref. [18]. For this reason, the CV-type model was extended to the description of deposition of binary alloy monolayers and submonolayers [29, 12, 13, 14, 15, 22, 23] and of thin films [48].

In the present work, we use kinetic Monte Carlo (KMC) simulations of a CV-type model to study the structure of thin films with two components in which the formation of domains of the same species is favored. The model parameters correspond to broad ranges of values of diffusion coefficients of adsorbed atoms, binding energies, and atomic fluxes, in order to explore possible properties of several materials and a variety of deposition conditions. We first consider the case of two species with similar dynamics, i.e. similar activation energy of terrace diffusion and similar binding energy. In a certain range of temperature and flux, it shows the formation of very large domains that meander across the film, connecting distant points, but have very narrow widths. We also consider the case of two species with different surface dynamics and show that the species with the largest mobility determines the conditions in which that domain morphology can be observed. Approximate relations for the domain widths are obtained in terms of the model parameters, which may help to obtain the desired nanoscale patterns in real films of two-component mixtures.

The rest of this paper is organized as follows. In Sec. 2, we present the deposition model, the simulation methods, and the main quantities to be measured. Sec. 3 presents the results for two species with similar surface dynamics and for two species with different surface dynamics in separate subsections, where the interpretations and consequences of the results are discussed. Sec. 5 summarizes our results and presents our conclusions.

2. Model and methods

2.1. Deposition model

The model is defined in a simple cubic lattice in which the edge of a site is taken as the unit length; thus, the values of lengths shown throughout this work are dimensionless. The substrate is initially flat, located at $z = 0$, and has lateral size L . Periodic boundary conditions are considered in x and y

directions. The two species of atoms/molecules are termed A and B particles; each deposited particle occupies one lattice site, independently of being A or B. We impose the solid-on-solid condition to the deposit, i.e. overhangs are not allowed. The set of particles with the same (x, y) positions is termed a column of the deposit.

Deposition occurs with a flux of particles in the z direction towards the substrate. The number of incident particles per column per unit time is F (unit s^{-1}). The probabilities of deposition of A and B particles are the same, so the films have an equimolar mixture. Adatom desorption is not considered in the model. We consider that mobile particles are only those at the top of each column.

Growth models that account for activated adatom diffusion of a single species usually consider that the hopping rate of the adatom can be written in the form $k = \nu \exp[-E_{act}/(k_B T)]$, where ν is a frequency (which depends on the temperature in the CV model [7]), E_{act} is an activation energy, k_B is the Boltzmann constant, and T is the temperature [18]. In the simplest cases, E_{act} has an additive form in terms of nearest neighbor (NN) interaction energies at the current position: $E_{act} = E_s + nE_b$, where E_s denotes the energy for diffusion on terraces and E_b denotes the bond energy with a lateral NN. The terrace diffusion coefficient is $D = \nu \exp[-E_s/(k_B T)]$. More realistic models also consider an additional energy barrier for crossing terrace edges [45], which leads to a probability for the hop to be executed to a lower or upper terrace.

In modeling two-component mixtures in the submonolayer regime, this approach was generalized to consider that E_s depends on the species of the mobile adatom and E_b is different for A-A, B-B, and A-B interactions [13]. In the case of thin films studied here, we have to consider that E_s depends on the species of the mobile adatom and on the species in terrace below that adatom.

These features can be summarized in a general expression for the rate at which a particle $p = \{A, B\}$ hops:

$$k_{pq n_A n_B}(T) = D_{pq}(\epsilon_{pA})^{n_A}(\epsilon_{pB})^{n_B}, \quad (1)$$

where:

$q = \{A, B, S\}$ denotes the site below p , which includes the possibility of substrate sites;

n_A and n_B are the number of lateral neighbors of species A and B, respectively;

$D_{pq} = (2k_B T/h) \exp \left[- \left(E_{pq}^{(ter)} \right) / (k_B T) \right]$ is the diffusion coefficient of particle p on a terrace with a particle q immediately below it (i.e. the hopping rate without lateral neighbors, $n_A = n_B = 0$), and $E_{pq}^{(ter)} > 0$ is the activation energy for this process;

$\epsilon_{pA} = \exp \left[- \left(E_{pA}^{(lat)} \right) / (k_B T) \right]$ and $\epsilon_{pB} = \exp \left[- \left(E_{pB}^{(lat)} \right) / (k_B T) \right]$, where $E_{pA}^{(lat)}$ and $E_{pB}^{(lat)}$ are bond energies with lateral neighbors A and B, respectively. Hereafter, the parameters ϵ_{pq} are termed detachment probabilities because their effects are to reduce the hopping rates when the adatoms have lateral neighbors.

In our model, we consider $E_{pq}^{(ter)} = E_{qp}^{(ter)}$ and $E_{pq}^{(lat)} = E_{qp}^{(lat)}$, which gives $D_{AB} = D_{BA}$ and $\epsilon_{AB} = \epsilon_{BA}$. Fig. 1 shows the hopping rates of mobile particles in some configurations.

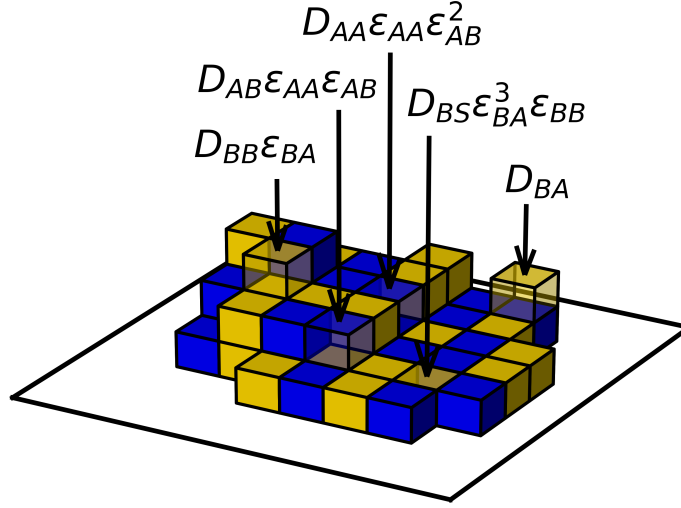


Figure 1: A small part of a deposit with A (blue) and B (yellow) particles and the hopping rates of some surface particles.

When a mobile particle hops, it moves to the top of a nearest neighbor column, which is randomly chosen among four directions, $(\pm x, \pm y)$. Upward and downward hops are allowed.

An additional energy barrier is considered when a particle attempts to hop to a layer at a different height z , which is the Ehrlich-Schwöebel barrier [45].

Here this mechanism is represented by a single probability P for any particle to hop to an upper or lower layer; with probability $1 - P$, the hop attempt is not executed. In all films studied here, local height differences are not large; thus, long distance hops in the vertical direction are not observed (if such hops were possible, then the probability of hopping to a different terrace should account for the diffusion along vertical walls and for the probable return to the original position; see Ref. [32]).

Here we consider cases in which the diffusion on terraces of a different species is faster than that on terraces of the same species, i.e. $D_{AB} > D_{AA}$ and $D_{AB} > D_{BB}$. This represents a weaker interaction between atoms of different species when compared to interactions of atoms of the same species. We also assume that interactions with the substrate are weak and set $D_{AS} = D_{BS} = D_{AB}$. Thus, D_{AB} is the parameter representing the largest hopping rates of the system, while the smaller values of D_{AA} and D_{BB} favor the formation of domains of the same species at the film surface.

In the CV model with a single species with terrace diffusion coefficient D , the main parameter is the dimensionless diffusion-to-deposition ratio $R = D/F$. Here, we extend that reasoning with the definition of three ratios:

$$R_{AA} = \frac{D_{AA}}{F} \quad , \quad R_{BB} = \frac{D_{BB}}{F} \quad , \quad R_{AB} = \frac{D_{AB}}{F}. \quad (2)$$

The remaining dimensionless parameters of the model in the present work are the detachment probabilities ϵ_{AA} , ϵ_{BB} , and ϵ_{AB} , and the jump probability P . These variables are more useful for the interpretation of scaling regimes than the sets of activation energies and temperature, as shown in works with a single atomic species [18, 8].

2.2. Simulation methods

We perform simulations on lattices with $L = 1024$, which are sufficiently large to represent many different microscopic environments in a single deposit. For most metals and semiconductors, this length corresponds to 0.2-0.3 μm . For each parameter set, we generated 10 deposits and observed small fluctuations in the average quantities; significant differences are observed only in the sizes of the largest clusters of A and B particles at large temperatures, but their orders of magnitude are the same in the different samples. The films typically have 30 deposited layers, which corresponds to thicknesses of order $\sim 10\text{nm}$ for metals or semiconductors.

The ratios R_{AA} and R_{BB} range between 10^4 and 10^7 , and the values of R_{AB} are 10-100 times larger than the largest single-species ratio (R_{AA} or R_{BB}). The values of ϵ_{AA} and ϵ_{BB} range between 10^{-5} and 10^{-2} . ϵ_{AB} is chosen in the range 10^{-2} - 10^{-1} to represent weak bonds between atoms of different species. The jump probability P is chosen in the range 10^{-3} - 10^{-1} .

Since the diffusion coefficients D_{pq} and the detachment probabilities ϵ_{pq} increase with temperature, it is interesting to compare results in which those parameters are simultaneously raised. For this reason, we performed several simulations with the conditions $R_{AB}/R_{AA} = \epsilon_{AB}/\epsilon_{AA}$, $R_{AB}/R_{BB} = \epsilon_{AB}/\epsilon_{BB}$, which correspond to $E_{AB}^{(ter)} - E_{AB}^{(lat)} = E_{AA}^{(ter)} - E_{AA}^{(lat)} = E_{BB}^{(ter)} - E_{BB}^{(lat)}$. However, we also performed simulations with parameters that are not constrained by these relations.

The simulations are implemented with an extension of the algorithm for a single species, which is described in detail in Ref. [31] and was formerly used in submonolayer growth simulations in our group [43].

The L^2 surface particles have their positions (x, y) grouped into ninety lists $X_{pq n_A n_B}$ according to the species ($p = A, B$), the type of the particle below it ($q = A, B, S$), the number of particles A at nearest-neighbor sites ($n_A = 0, \dots, 4$) and the number of particles B at nearest-neighbor sites ($n_B = 0, \dots, 4$), with the latter numbers constrained to $0 \leq n_A + n_B \leq 4$. The position of a surface particle in a list $X_{pq n_A n_B}$ is stored in an inverted-list matrix $M_1(x, y)$. In addition, a matrix $M_2(x, y, z)$ stores the particles (A or B) and empty sites, with $M_2(x, y, 0) = S$, and is used for rapid access to the configuration of the neighborhood of a mobile particle.

At each step of the simulation, the rates of all possible events (namely, deposition of A, deposition of B, and hop of one of the L^2 surface particles) are calculated and their sum is denoted as Σ . The probability of each deposition event is the ratio between its rate and Σ . Since all particles in each list $X_{pq n_A n_B}$ have the same hopping rate, the probability of that list is the product of the number of particles in the list and the hopping rate divided by Σ . The event to be executed is then chosen according to those probabilities. In the case of choosing a list, one of its particles is randomly chosen to hop, in a direction which is also randomly chosen among four possibilities ($\pm x, \pm y$); in the case of a hop to a different layer, the hop is executed with probability P , otherwise nothing occurs.

After a simulation step, the time is incremented by $1/\Sigma$ minus the natural logarithm of a randomly chosen number in the interval $(0, 1]$; the latter

contribution has very small effect on the total deposition time.

2.3. Basic quantities

The fluctuations of the surfaces of the growing films are monitored with the calculation of the roughness, which is defined as

$$W(L, t) \equiv \left\langle \left[\overline{(h - \bar{h})^2} \right]^{1/2} \right\rangle, \quad (3)$$

where the overbars indicate spatial averages and the angular brackets indicate configurational averages. Since W accounts for height fluctuations in the whole film surface, it is frequently called global roughness; the local asperity of the surface is sometimes quantified by the local surface roughness [6].

Visual inspection of cross sections of the deposited films showed meandering domains of both species. To characterize these domains, we calculate characteristic lengths and areas in horizontal cross sections at heights $z = 5, 10, 15,$ and 20 . The distributions of domain area S of both species, $P_A(S)$ and $P_B(S)$, are calculated using the Hoshen-Kopelman algorithm for identification of connected clusters [46].

For the calculation of domain widths, in each line of constant x or y , we measure the size of all segments of consecutive sites of the same species. This is equivalent to the definition of a spatial persistence length in one-dimensional interface problems [38]. The average values of those segment sizes are defined as the domain widths λ_A and λ_B ; in cases where A and B interactions are similar, the average domain width is $\lambda = (\lambda_A + \lambda_B)/2$.

3. Results

3.1. Two species with the same surface mobility

Here we analyze data for $R_{AA} = R_{BB}$ and $\epsilon_{AA} = \epsilon_{BB}$, which is hereafter termed symmetric case. It represents mixtures of two species that have similar values of activation energy of surface diffusion and of bond energy.

3.1.1. Low temperatures

Here we consider $R_{AA} = 10^4$, which is typical of low temperatures. For atoms with $E_{AA}^{(ter)} \approx 0.5eV$ and a flux of ~ 1 monolayer per second, this is obtained close to room temperature. For some metals with very small activation barriers of surface diffusion (e.g. $E_{AA}^{(ter)} \sim 0.2eV$ [18]), this corresponds

to much lower temperatures. The values of ϵ_{AA} are also expected to be small in these conditions; for instance, with a low value $E_{AA}^{(lat)} \sim 0.2eV$ and at room temperature, we have $\epsilon_{AA} \sim 10^{-3}$.

Fig. 2(a) shows vertical cross sections of films with $R_{AB} = 10^6$, $\epsilon_{AB} = 0.1$, $\epsilon_{AA} = 10^{-3}$, and $P = 10^{-3}$. Fig. 2(b) shows vertical cross sections of films with $R_{AB} = 10^5$, $\epsilon_{AB} = 0.1$, $\epsilon_{AA} = 10^{-2}$, and $P = 10^{-1}$. The values of the surface roughness W , which are shown below those images, illustrate the general trend of W to increase as P decreases. This parallels the observations in films with a single species [18, 32]. In both cases, we observe the formation of disordered narrow domains; some of those domains connect the substrate and the top surface.

Figs. 2(c) and 2(d) show horizontal cross sections at height $z = 10$ of films deposited with the same parameters of Figs. 2(a) and 2(b), respectively. The average domain width λ is indicated below those plots and quantitatively confirm that the domains are very narrow. Figs. 2(e) and 2(f) show the corresponding distributions of domain size at height $z = 10$ (recall that A and B are equivalent in this case). The distributions obtained at $z = 15$ were similar.

These distributions have a decreasing part with average $\langle S \rangle \sim 10^2$, which corresponds to small domains of A and B with randomly distributed sizes. However, they also have peaks at a size $S \sim 10^6$, which is indicated by arrows in Figs. 2(e) and 2(f) and appears in all samples simulated in these low temperature conditions. This indicates that the films have large domains of A and B crossing it in the horizontal directions; the particles belonging to the largest A domain in Figs. 2(c) and 2(d) are highlighted. That domain meanders across the sample with a very irregular shape and a very narrow and fluctuating width, which is confirmed by the small value λ .

We also deposited films with $R_{AA} = 10^4$ and other five different sets of parameters. The results are similar to those shown in Figs. 2(a)-(f): the films have large domains, with total sizes of order $S \sim 10^6$, but the average widths λ vary between 2.7 and 4.2, which corresponds to sizes $\sim 1nm$ for metals and semiconductors. No significant effect of R_{AB} , ϵ_{AB} , or ϵ_{AA} is observed.

It is important to observe that the formation of long connected domains in a square grid, which is the case of the horizontal sections of Figs. 2(b) and 2(d), is not possible if the distribution of the two species is random because a 50-50 mixture is below the critical percolation point [46]. Thus, the observed connectivity represents a long-range correlation of atomic positions.

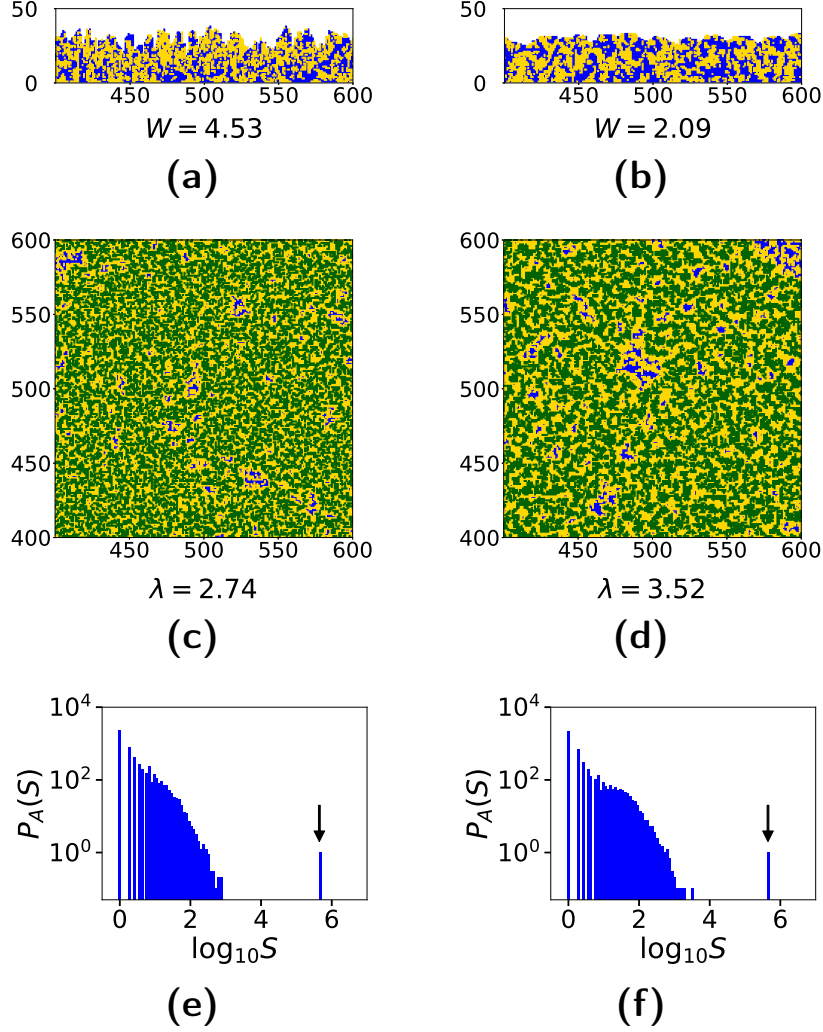


Figure 2: (a) Vertical cross sections, (c) horizontal cross sections at $z = 10$, and (e) domain size distribution at $z = 10$ of films deposited with $R_{AA} = 10^4$, $\epsilon_{AA} = 10^{-3}$, $R_{AB} = 10^6$, $\epsilon_{AB} = 0.1$, and $P = 10^{-3}$. (b) Vertical cross sections, (d) horizontal cross sections at $z = 10$, and (f) domain size distribution at $z = 10$ of films deposited with $R_{AA} = 10^4$, $\epsilon_{AA} = 10^{-2}$, $R_{AB} = 10^5$, $\epsilon_{AB} = 0.1$, and $P = 10^{-1}$. A particles are in blue, B in yellow, and the largest domain of A is in green in (c) and (d). The surface roughness is indicated in (a) and (b), and the average domain sizes are indicated in (c) and (d). In (e) and (f), the arrows indicate the largest domain sizes.

3.1.2. Effects of the diffusion coefficient on terraces of a different species

Here we analyze the effects of the diffusion coefficient D_{AB} of a particle on a terrace of a different species, i.e. A on a terrace of B or vice-versa. This is possible by varying R_{AB} while the other model parameters are kept fixed. Note that D_{AB} is set equal to D_{AS} , which controls the formation of islands in the submonolayer regime because they predominantly grow by capturing freely moving adatoms [18]. We consider cases of non-negligible barriers for crossing terrace edges: $P \leq 10^{-2}$.

Fig. 3(a) shows vertical and horizontal ($z = 10$) cross sections and the domain size distribution of films grown with $R_{AA} = 10^5$, $\epsilon_{AA} = 10^{-2}$, $P = 10^{-3}$, $\epsilon_{AB} = 0.1$, and $R_{AB} = 10^6$. For comparison, Fig. 3(b) shows cross sections and distributions of films grown with the same parameters except $R_{AB} = 10^8$. Domain size distributions obtained at $z = 10$ and $z = 15$ were similar in all cases.

Again we observe the formation of very large horizontal domains ($S \sim 10^6$) in all films, but with very small average widths $\lambda \sim 5$. These results show that D_{AB} has small effects on the domain size at layers $z \geq 10$. The vertical cross sections in Figs. 3(a),(b) show that the only significant effect of D_{AB} is to improve the vertical orientation of the domains, so that their meandering at a given height is strongly correlated with the meandering at the layer below it.

Similar conclusions are obtained by comparing films whose data are shown in Figs. 4(a) ($R_{AB} = 10^8$) and 4(b) ($R_{AB} = 10^9$), in which the other parameters are $R_{AA} = 10^7$, $\epsilon_{AA} = 10^{-3}$, $P = 10^{-2}$, and $\epsilon_{AB} = 0.1$. Note that the domain widths are much larger in this case if compared to Figs. 3(a),(b).

The diffusion coefficients $D_{AB} = D_{BA} = D_{AS} = D_{BS}$ also have weak effect on the domain sizes and widths in other films in which only these parameters were changed and in which the energies of step barriers are large (small P). However, in Sec. 3.1.5, we will show that D_{AB} plays a role in cases with $P = 0.1$, which is important for high temperature deposition.

We recall that the island density in submonolayer island growth with two species is predominantly affected by the diffusion coefficients of those species on the substrate [13, 14]. Thus, the results of this section show that the effects of the short range interactions with the substrate propagate only to a small number of atomic layers in conditions of low to intermediate temperatures.

3.1.3. Effects of the diffusion coefficient on terraces of the same species

Here we analyze the role of $R_{AA} = D_{AA}/F$ on the film structure.

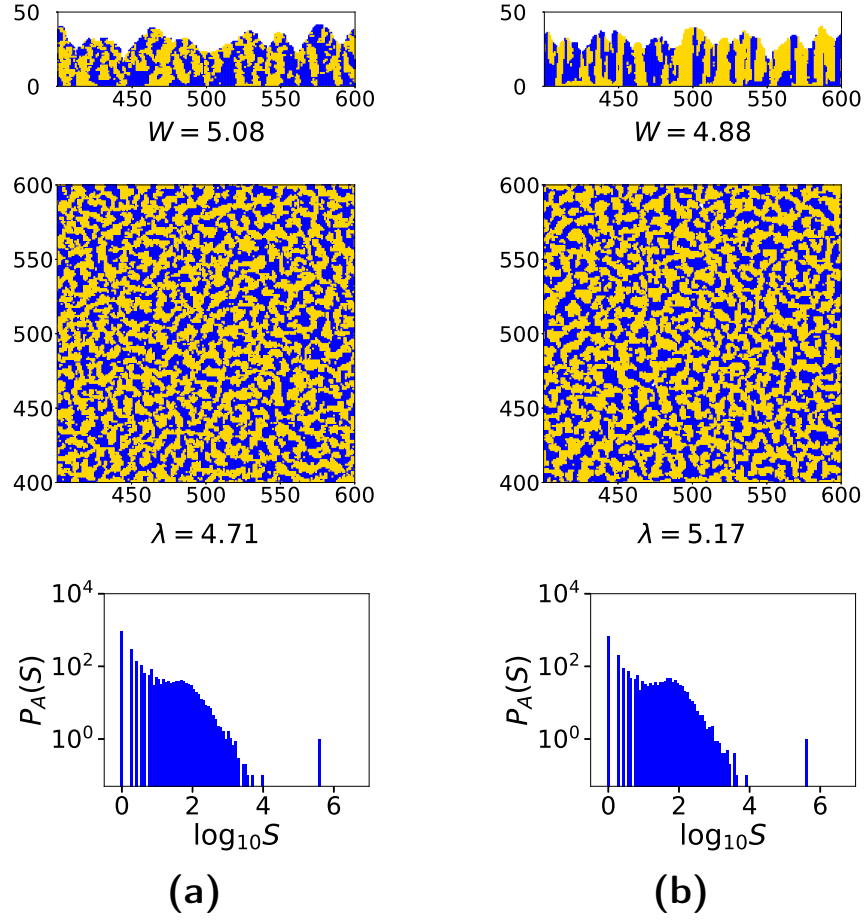


Figure 3: Vertical cross sections, horizontal cross sections at $z = 10$, and A domain size distributions at $z = 10$ in films deposited with $R_{AA} = 10^5$, $\epsilon_{AA} = 10^{-2}$, $\epsilon_{AB} = 0.1$, $P = 10^{-3}$, and: (a) $R_{AB} = 10^6$; (b) $R_{AB} = 10^8$. A particles are in blue, B in yellow. The surface roughness and the average domain sizes in the cross sections at $z = 10$ are indicated.

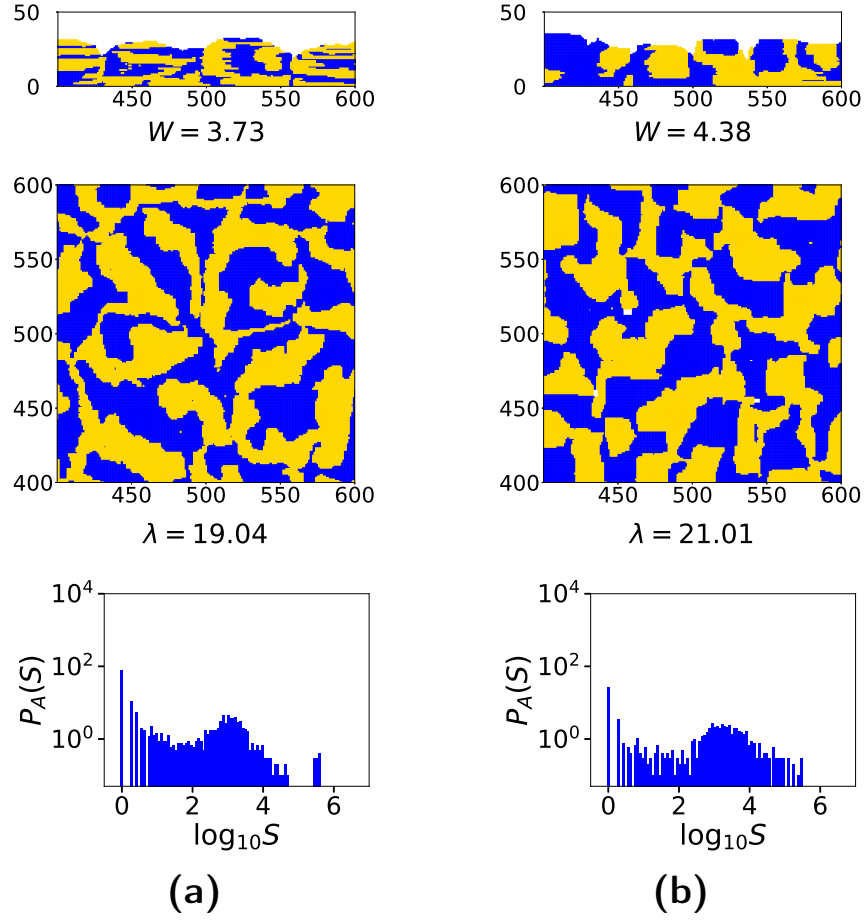


Figure 4: Vertical cross sections, horizontal cross sections at $z = 10$, and A domain size distributions at $z = 10$ in films deposited with $R_{AA} = 10^7$, $\epsilon_{AA} = 10^{-3}$, $\epsilon_{AB} = 0.1$, $P = 10^{-2}$, and: (a) $R_{AB} = 10^8$; (b) $R_{AB} = 10^9$. A particles are in blue, B in yellow. The surface roughness and the average domain sizes in the cross sections at $z = 10$ are indicated.

Fig. 5(a) shows cross sections and domain size distributions of films grown with $R_{AA} = 10^5$ and $R_{AB} = 10^7$; Fig. 5(b) shows cross sections and domain size distributions of films grown with $R_{AA} = 10^6$ and $R_{AB} = 10^8$. The remaining parameters in Figs. 4(a) and 4(b) are the same: $\epsilon_{AA} = 10^{-3}$, $P = 10^{-2}$, and $\epsilon_{AB} = 0.1$.

The change of two orders of magnitude in R_{AA} (from 10^5 to 10^7) does not lead to a significant change in the surface roughness W . In deposition of films with a single species and no step barrier, $W < 1$ at short times for $10^5 \leq R \leq 10^7$, i.e. the films have very smooth surfaces [8]. Consequently, we actually do not expect that the relatively larger values of W shown in Figs. 4 and 5 are related to the values of R_{AA} .

On the other hand, the average width of the domains increases with R_{AA} : as this ratio varies from 10^5 [Fig. 5(a)] to 10^7 [Fig. 4(a),(b)], that width increases by a factor between 4 and 5. Indeed, a larger mobility on the terrace of a domain facilitates its lateral expansion. Figs. 5(a),(b) shows that this large mobility works against the vertical alignment of the domains, which is consistent with the interpretation of a facilitated lateral propagation.

The cluster size distributions for $R_{AA} \geq 10^5$ differ from those of low temperatures (Sec. 3.1.1) because they have a peak at a finite size, which moves from $S \sim 10^2$ in $R_{AA} = 10^5$ to $S \sim 10^3$ in $R_{AA} = 10^7$. This means that the small domains have a characteristic size; some of those domains can be observed in the horizontal cross sections of Figs. 4(a) and 4(b), in which R_{AA} is large. The sizes of the largest domains decrease as R_{AA} increases: for $R_{AA} \leq 10^6$ [Figs. 5(a),(b)], the largest domains have $S \sim 10^6$, but for $R_{AA} = 10^7$ [Fig. 4(b)], they have $S \sim 10^5$. This indicates that the increase of the size of finite domains, which is a signature of enhanced phase separation, is accompanied by a decrease in the long distance connectivity of the largest domains across the film.

3.1.4. Effects of lateral interactions of the same species

Now we analyze the role of the detachment probability ϵ_{AA} on the film structure. We compare the structures of films grown with constant values $R_{AA} = 10^6$, $P = 10^{-2}$, and $\epsilon_{AB} = 0.1$. The values of R_{AB} are in the range 10^7 - 10^8 , but the effect of this change is negligible, as discussed in Sec. 3.1.2.

Figs. 6(a) and 6(b) show cross sections and domain size distributions of films grown with $\epsilon_{AA} = 10^{-2}$ ($R_{AB} = 10^7$) and $\epsilon_{AA} = 10^{-4}$ ($R_{AB} = 10^8$). For comparison, consider the data shown in Fig. 5(b) for an intermediate probability $\epsilon_{AA} = 10^{-3}$ ($R_{AB} = 10^8$).

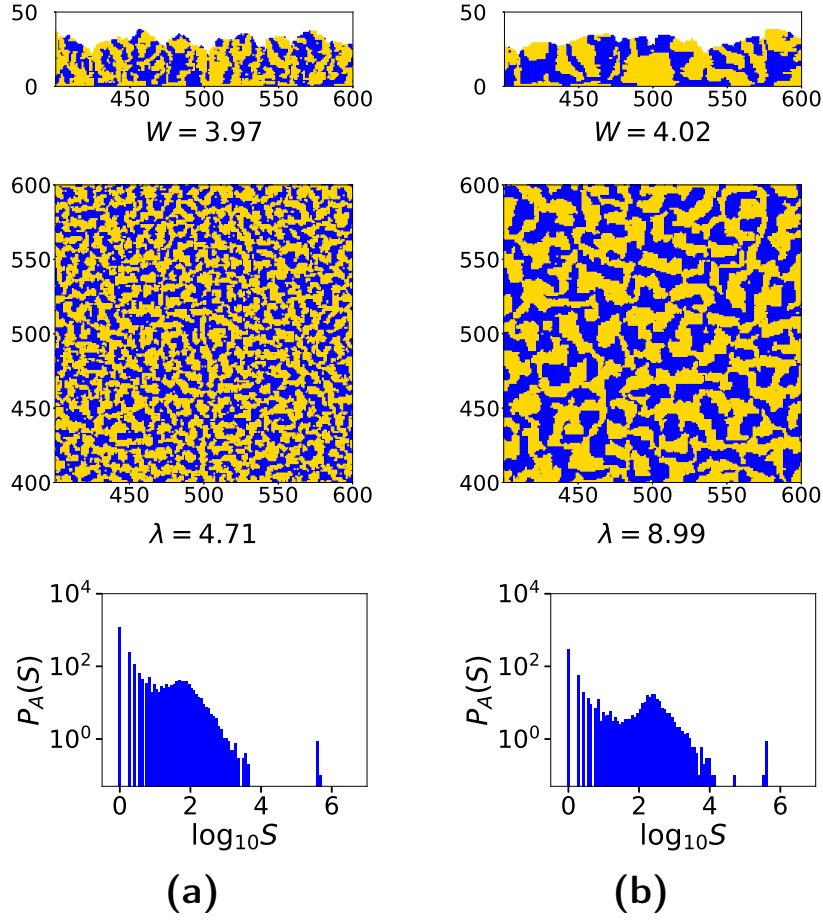


Figure 5: Vertical cross sections, horizontal cross sections at $z = 10$, and A domain size distributions at $z = 10$ in films deposited with $\epsilon_{AA} = 10^{-3}$, $\epsilon_{AB} = 0.1$, $P = 10^{-2}$, and: (a) $R_{AA} = 10^5$, $R_{AB} = 10^7$; (b) $R_{AA} = 10^6$, $R_{AB} = 10^8$. A particles are in blue, B in yellow. The surface roughness and the average domain sizes in the cross sections at $z = 10$ are indicated.

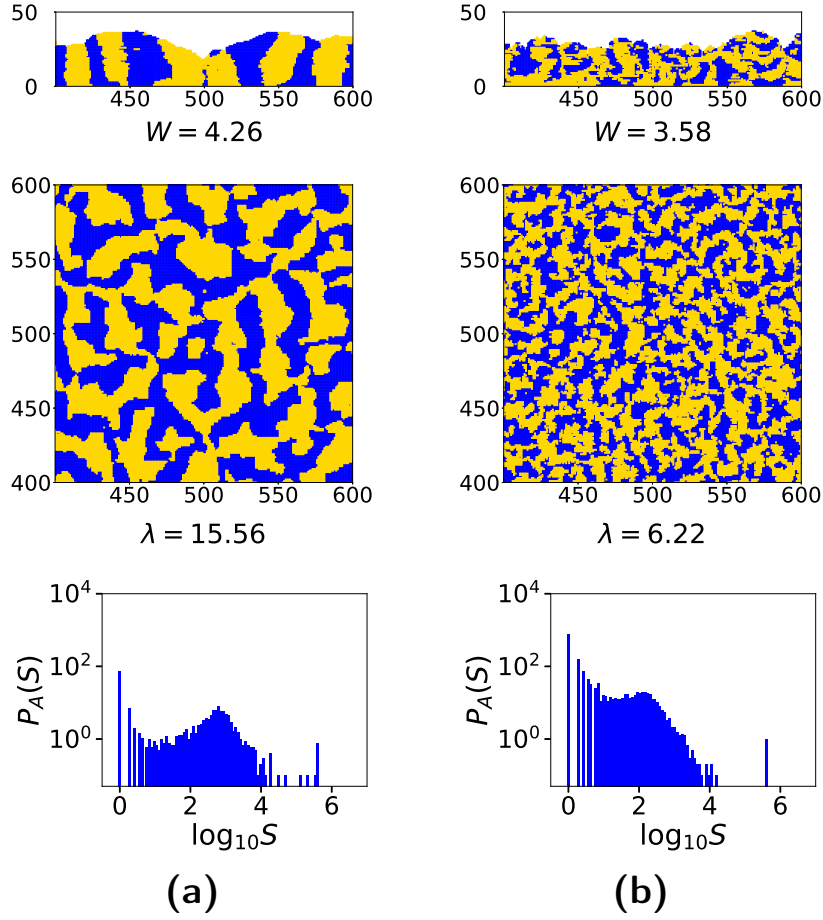


Figure 6: Vertical cross sections, horizontal cross sections at $z = 10$, and A domain size distributions at $z = 10$ in films deposited with $R_{AA} = 10^6$, $\epsilon_{AB} = 0.1$, $P = 10^{-2}$, and: (a) $\epsilon_{AA} = 10^{-2}$, $R_{AB} = 10^7$; (b) $\epsilon_{AA} = 10^{-4}$, $R_{AB} = 10^8$. A particles are in blue, B in yellow. The surface roughness and the average domain sizes in the cross sections at $z = 10$ are indicated.

The effect of ϵ_{AA} on the surface roughness is small; this is also observed in films with a single species [8]. However, the vertical and horizontal cross sections show that the domain width significantly increases as ϵ_{AA} increases: when this parameter varies from 10^{-4} to 10^{-2} , that width changes by a factor near 2.5. The increase of ϵ_{AA} also leads to an increase in the average size of the finite domains, which are of order $S \sim 10^2$ for $\epsilon_{AA} = 10^{-4}$ and $S \sim 10^3$ for $\epsilon_{AA} = 10^{-2}$.

The vertical cross sections also show that the increase of ϵ_{AA} improves the vertical domain orientation. This is also observed with other values of R_{AA} , from 10^5 to 10^7 , and with other values of P , from 10^{-1} to 10^{-3} .

Work on deposition of films with a single species showed that the increase of the detachment probability from lateral neighbors (ϵ) leads to the formation of more compact islands and smoother terrace borders [51]. Conversely, decreasing ϵ leads to more branched islands and terraces because the branches typically have atoms with low coordination. With two species, the branching mechanism facilitates the lateral propagation of a domain over a domain of the other species; consequently, decreasing ϵ_{AA} contributes to destroy the vertical orientation, as observed in the simulations.

3.1.5. Effects of step energy barriers

The increase of P means that it becomes easier for a particle to jump between different heights, upward or downward. For a given step energy barrier, P increases with the temperature.

Figs. 7(a) and 7(b) show cross sections and domain size distributions of films grown with $P = 10^{-1}$ and $P = 10^{-3}$, respectively, in both cases with $R_{AA} = 10^7$, $R_{AB} = 10^9$, $\epsilon_{AB} = 10^{-1}$, and $\epsilon_{AA} = 10^{-3}$. They can be compared with the data in Fig. 4(b), in which $P = 10^{-2}$ and the other parameters have the same values as here.

The vertical cross sections show that the film surface is locally smoother as P increases. However, the large values of the roughness W in Figs. 7(a),(b) do not seem to be consistent with this result. The reason is that W is affected by the large height differences between some domains when $P = 10^{-1}$; this leads to the formation of the gaps observed in the horizontal cross sections of Fig. 7(a). Increasing P also leads to the increase of the width of the domains and to the enhancement of the vertical orientation, which are effects similar to those of the detachment probability ϵ_{AA} .

The distributions of domain sizes show that, as P increases, the peak corresponding to finite domains shifts from $S \sim 10^3$ ($P = 10^{-3}$) to $S \sim$

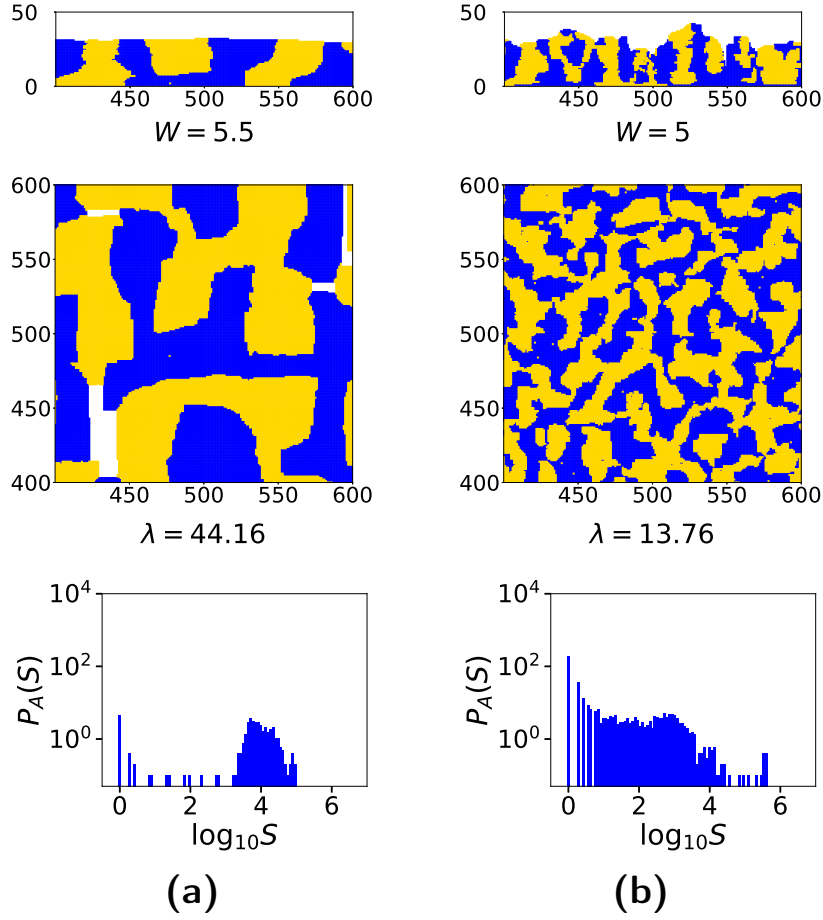


Figure 7: Vertical cross sections, horizontal cross sections at $z = 10$, and A domain size distributions at $z = 10$ in films deposited with $R_{AA} = 10^7$, $R_{AB} = 10^9$, $\epsilon_{AA} = 10^{-3}$, $\epsilon_{AB} = 10^{-1}$, and: (a) $P = 10^{-1}$; (b) $P = 10^{-3}$. A particles are in blue, B in yellow. The surface roughness and the average domain sizes in the cross sections at $z = 10$ are indicated.

10^4 ($P = 10^{-1}$). The increase in the size of finite domains is accompanied by a decrease in the size of the largest domain. Careful inspection of Fig. 7(a) ($P = 10^{-1}$) shows that A and B domains do not connect the opposite boundaries of the image; at some points, they are separated by gaps because the layer $z = 10$ is not completely filled. This indicates the loss of long range connectivity of this largest cluster in conditions of high temperatures or in cases where the energy barriers at edges are very small (large P).

3.1.6. High temperature deposition

The separate analysis of the effects of each model parameter in the previous sections can be used to provide a consistent picture of the structure of the binary films deposited at high temperatures. This regime corresponds to large values of the diffusion coefficients, detachment probabilities, and step jump probability. The results in Fig. 7(a) are helpful at this point. The general trend is that the film surfaces become locally smoother and that the domains have larger widths. However, the size of the largest clusters decreases and the long range connectivity may be lost.

The diffusion coefficients on terraces of different species are also large at high temperatures. This contributes to the formation of large islands on the substrate, which subsequently leads to the formation of large compact domains with gaps between them.

Our simulations for $P = 10^{-1}$ also show that the average domain width has a non-negligible increase as R_{AB} increases. This contrasts with the results of Sec. 3.1.2 for small P .

We conclude that the formation of long connected domains with non-negligible width is possible in a narrow range of parameters. In the present model, this range is represented by most of our results with $R_{AA} = 10^5$ - 10^6 (except those with very small P or ϵ_{AA}), and the results with $R_{AA} = 10^7$, $P \leq 10^{-2}$, and $\epsilon_{AA} \leq 10^{-2}$. Thus, the appropriate tuning of temperature and flux is necessary for production of films with long enough domains that cross it in the horizontal directions with a nanometer size width.

3.1.7. Scaling of the average domain width

Considering the observed effects of model parameters on the average domain width, we searched for a quantitative relation between them. A simple approximate relation is proposed with the form

$$\lambda \approx A[R_{AA}\epsilon_{AA}^x P^y]^\gamma, \quad (4)$$

in which the prefactor A and the exponents x , y , and γ are to be determined. Here we will show data obtained in $z = 10$, but the values obtained in $z = 15$ are similar.

We first consider data with non-negligible terrace edge barriers, $P \leq 10^{-2}$. Plots of $\log \lambda$ as a function of $\log [R_{AA}\epsilon_{AA}^x P^y]$ were constructed with several choices of x and y . The best data collapse is obtained with $x = 0.7$ and $y = 0.4$, as shown in Fig. 8(a). It also shows a linear fit of the data with large values in the abscissa, which gives $\gamma \approx 0.39$ and $A \approx 0.5$.

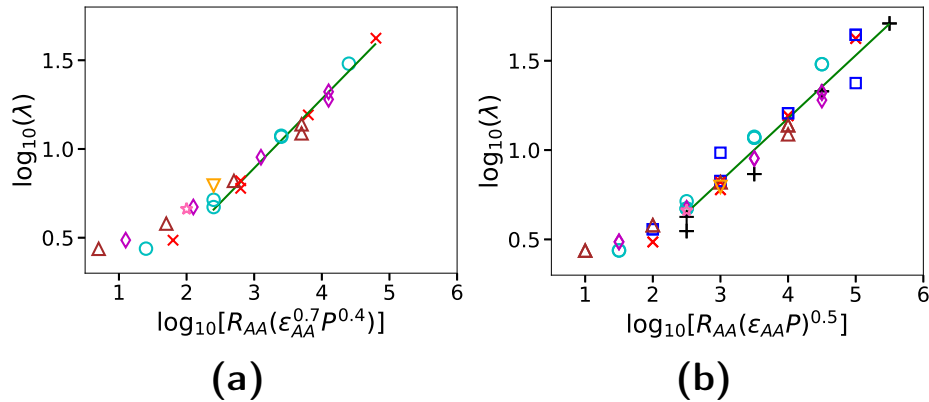


Figure 8: Scaling plots of the average domain width at $z = 10$ with (a) $P \leq 10^{-2}$ and (b) all simulated values of P . Different symbols correspond to different combinations of the parameters. The values of (ϵ_{AA}, P) for each symbol are: plus sign ($10^{-2}, 10^{-1}$); crosses ($10^{-2}, 10^{-2}$); circles ($10^{-2}, 10^{-3}$); squares ($10^{-3}, 10^{-1}$); diamonds ($10^{-3}, 10^{-2}$); triangles ($10^{-3}, 10^{-3}$); inverted triangles ($10^{-4}, 10^{-2}$); stars ($10^{-4}, 10^{-3}$). The solid lines are linear fits of the data with $\lambda \geq 5$ with slopes (a) 0.39 and (b) 0.35.

If we include data with small terrace edge barriers ($P = 10^{-1}$), the dispersion of the data is larger for any choice of x and y . The best data collapse is now obtained with $x = 0.5$ and $y = 0.5$, as shown in Fig. 8(b). However, the linear fit of the data with $\lambda \geq 5$ has a slope $\gamma \approx 0.35$ and the prefactor is $A \approx 0.6$, which are not very different from the previous estimates.

The values of D_{AA} , ϵ_{AA} , and P for various metals and semiconductors with different surface orientations are given in the literature; see e.g. Ref. [18]. For a given binary mixture, those data and the fits shown in Figs. 8(a),(b) may help to predict the order of magnitude of the size of nanoscale domains formed in films of that mixture.

3.2. Two species with different surface mobilities

Now we consider cases with very different mobilities of A and B in terraces of the same species, which are represented by $R_{AA} = 100R_{BB}$. The probabilities of detachment from lateral neighbors follow the same relation. The diffusion coefficients in terraces of a different species are much larger than both D_{AA} and D_{BB} , which contributes to the domain separation.

The inspection of several data sets shows some qualitative trends that are similar to those of the case with equal mobilities of the two species. First, the roughness decreases as R_{AA} or R_{BB} increase and as P increases. Second, the average domain width increases with the increase of all the main model parameters: R_{AA} , R_{BB} , ϵ_{AA} , ϵ_{BB} , and P .

To investigate the case of low to intermediate temperatures, in Fig. 9 we show vertical and horizontal cross sections of the deposits and the distributions of sizes of domains A and B at $z = 15$, for films grown with: $R_{AA} = 10^6$, $R_{BB} = 10^4$, $R_{AB} = 10^8$, $\epsilon_{AA} = 10^{-3}$, $\epsilon_{BB} = 10^{-5}$, $\epsilon_{AB} = 10^{-1}$, and $P = 10^{-2}$. The distribution of A shows a large domain ($S \sim 10^6$) at $z = 15$ and at other heights. The largest domains of B have $S \sim 10^5$; at $z = 10$, their areas are smaller than 10^5 . The size distributions of both A and B are superpositions of a monotonically decreasing part and a peaked part; the peak of A is located at a size smaller than 10^2 and the peak of B is near size 10^2 . This indicates a trend that the most mobile species (A) forms the largest domain, which connects long distances, while the less mobile species (B) forms finite domains with areas typically larger than the other one.

The domain size distributions of A and B are different from those of the symmetric case with $R_{AA} = R_{BB} = 10^4$ [Figs. 2(e)-(f)] and with $R_{AA} = R_{BB} = 10^6$ [Figs. 5(b), 6(a)-(b)]. Here, the distribution of A is similar to the distribution obtained in the symmetric case with $R_{AA} = R_{BB} = 10^5$ [Fig. 5(a)], i.e. with a diffusion-to-deposition ratio intermediate between those of A and B in the asymmetric case. The comparison of horizontal cross sections in Figs. 5(a) and 9 visually confirms that the domain morphologies are similar.

A case of intermediate to high temperature is shown in Fig. 10. At or below $z = 10$, a very large domain of species B is formed, but not of A; the situation changes at or above $z = 15$, in which there is a large domain of A but not of B. The horizontal cross section at $z = 10$ confirms that finite domains of A are surrounded by a narrower domain of B which connects the external borders of that image; the inverse occurs at $z \geq 15$.

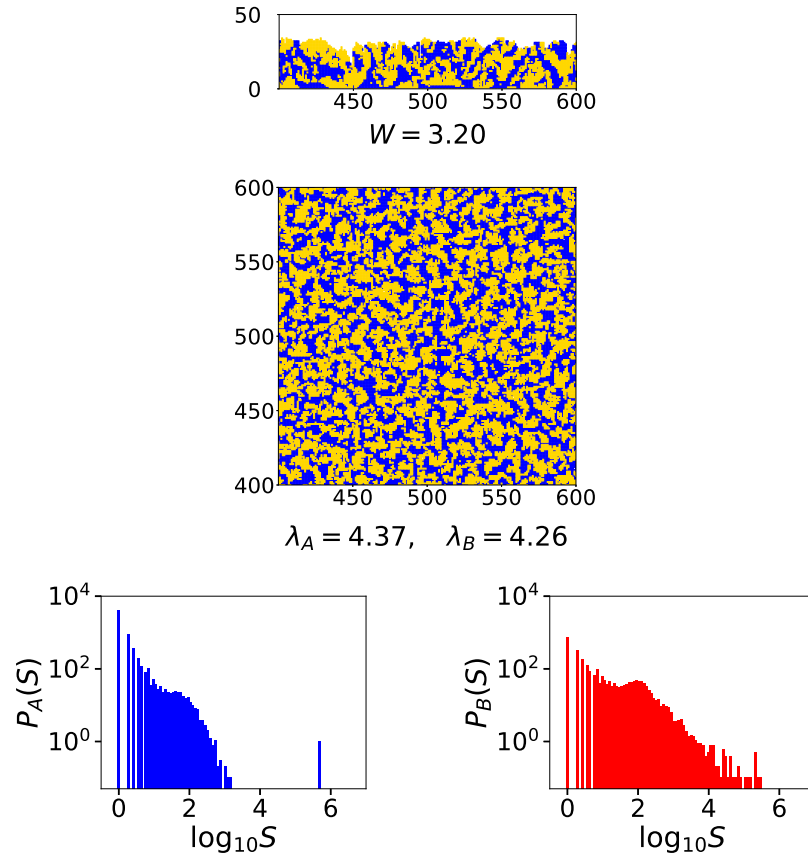


Figure 9: Vertical cross section, horizontal cross section at $z = 15$, and domain size distributions of A and B at $z = 15$ in films deposited with $R_{AA} = 10^6$, $R_{BB} = 10^4$, $R_{AB} = 10^8$, $\epsilon_{AA} = 10^{-3}$, $\epsilon_{BB} = 10^{-5}$, $\epsilon_{AB} = 10^{-1}$, $P = 10^{-2}$. A particles are in blue, B in yellow. The surface roughness and the average domain sizes in the horizontal cross section are indicated.

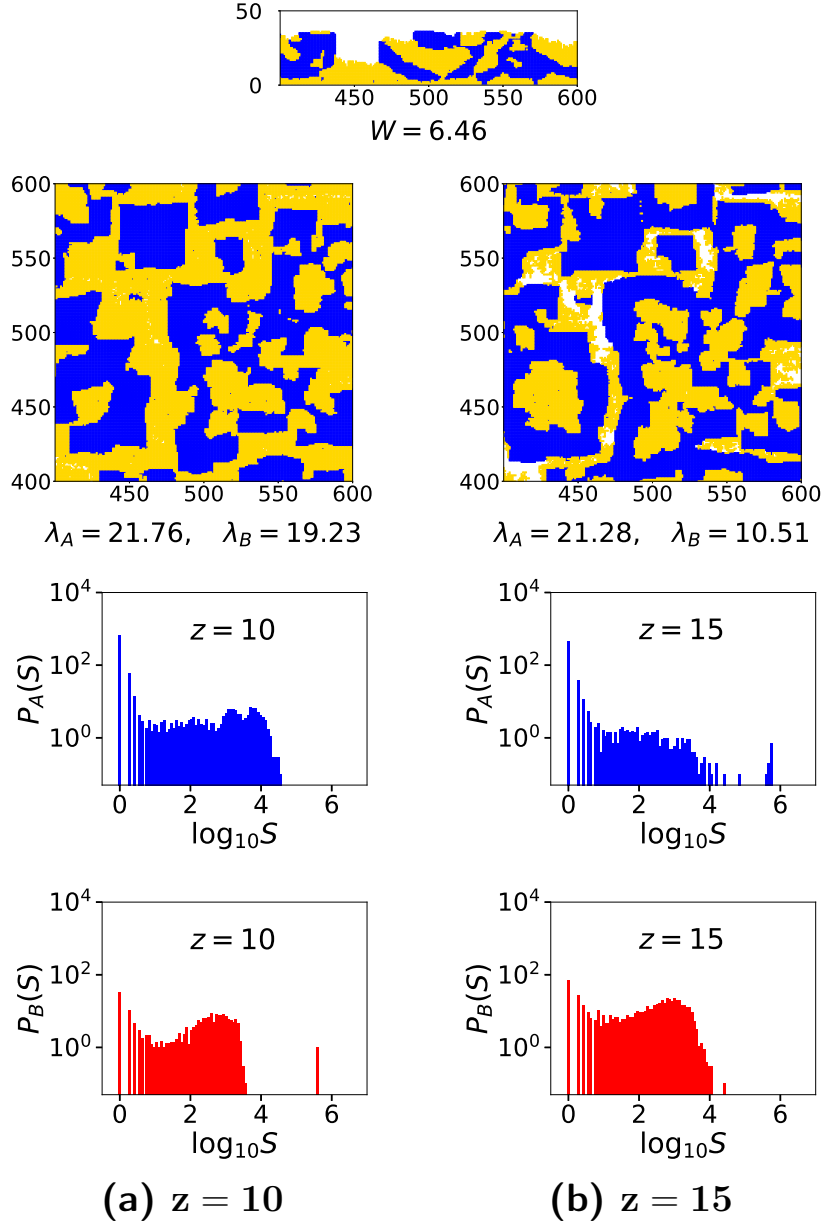


Figure 10: Vertical cross section of a film deposited with $R_{AA} = 10^7$, $R_{BB} = 10^5$, $R_{AB} = 10^9$, $\epsilon_{AA} = 10^{-3}$, $\epsilon_{BB} = 10^{-5}$, $\epsilon_{AB} = 10^{-1}$, and $P = 10^{-1}$. (a) and (b) show horizontal cross section and domain size distributions at $z = 10$ and $z = 15$, respectively. A particles are in blue, B in yellow. The surface roughness and the average domain sizes in the horizontal cross section are indicated.

The film structure in Fig. 10 resembles that of the symmetric case in Fig. 7(a), in which $R_{AA} = R_{BB} = 10^7$, $\epsilon_{AA} = \epsilon_{BB} = 10^{-3}$, and $P = 0.1$. Thus, in intermediate to high temperatures, the structure is similar to that obtained with two similar species with the largest mobility. This suggests that the most mobile species is responsible for the loss of long range domain connectivity at high temperatures.

We also tried to fit the data for this case with a relation similar to Eq. (4), but using a ratio R and a probability ϵ equal to the geometric means of their values for A and B species. Figs. 11(a) and 11(b) show domain widths λ_A and λ_B obtained at $z = 10$, respectively, as a function of the appropriate scaling variable, in cases with $R_{AA}/R_{BB} = 10$ (small difference between the surface diffusivities of A and B). Figs. 11(c) and 11(d) show the same quantities in cases with $R_{AA}/R_{BB} = 100$.

We observe that the scatter of the data is smaller for $R_{AA}/R_{BB} = 10$. The fits in Figs. 11(a),(b) give

$$\lambda_A \approx A_1 [R_{AA}R_{BB}(\epsilon_{AA}\epsilon_{BB})^{0.5}P]^\delta \quad , \quad \lambda_B \approx B_1 [R_{AA}R_{BB}(\epsilon_{AA}\epsilon_{BB})^{0.5}P]^\delta \quad (5)$$

with $\delta \approx 0.2$, $A_1 \approx 0.4$, and $B_1 \approx 0.4$. This shows that a difference of one order of magnitude in surface diffusion coefficients and lateral detachment probabilities do not change the main conclusions obtained in the symmetric case of Sec. 3.1. However, for $R_{AA}/R_{BB} = 100$, we have already observed that characteristic sizes of the domains of the two species are very different, which explains why it is difficult to collapse data of different species with a single scaling variable.

4. Discussion

The deposition of thin films with two-component mixtures was simulated and the effects of the terrace diffusion coefficients, the probabilities of detachment from island and terrace borders, and the barriers for crossing terrace edges were analyzed. Some features of the model are similar to those of previous models of submonolayer growth of binary mixtures [13, 14]; however, the main difference here is that the surface diffusion coefficient of a given species also depends on the terrace where it is moving. In all cases, we considered that the surface mobility of a given species is larger (possibly much larger) in terraces of the other species in comparison with the mobility in terraces of the same species, which is beneficial to the separation of domains.

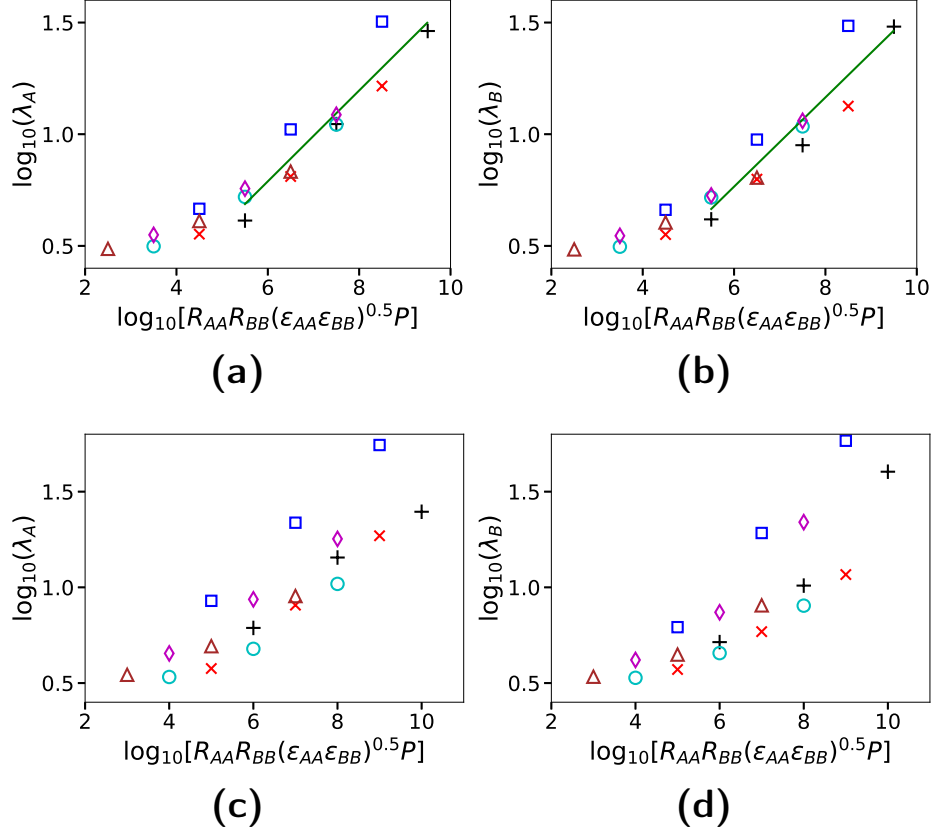


Figure 11: Average domain widths of species A and B for: (a),(b) $R_{AA}/R_{BB} = 10$; (c),(d) $R_{AA}/R_{BB} = 100$. Each symbol corresponds to a different parameter set. The solid lines in (a) and (b) are linear fits of the data with $\lambda \geq 5$.

Most of our simulations considered the case of two species with approximately the same activation energies for terrace diffusion and for detachment from lateral neighbors. When terrace diffusion coefficients differ by a factor 10, the results are similar. The effects of increasing temperature summarized below must be understood as effects of increasing the diffusion-to-deposition ratios, so that similar effects can be obtained by decreasing the deposition rate.

For low and intermediate temperatures, we observe the formation of very narrow domains with highly disordered shape; for metals and semiconductors, the domain widths are of some nanometers. Those domains occupy a

large fraction of horizontal cross sections, so that they connect very distant points across the substrate directions. The scaling of the average width obtained here involves only parameters describing the interactions of a single species, which depend on activation energies for surface diffusion and on the temperature. The leading contribution comes from terrace diffusion. Since the values of activation energies of this process were already obtained by experimental and *ab initio* calculations for several materials and deposition conditions [18], they may be used to predict the domain widths of real binary mixtures. Note that most metals and semiconductors have lattice structure different from the simple cubic model considered here, but the present scaling relations may be reasonable to predict the orders of magnitude of domain widths.

The long range domain connectivity may be interesting for the production of multifunctional materials if the two deposited species have different thermal, electric, or magnetic properties. In alloys where previous works showed the formation of lamellar domains in the nanoscale, the investigation of their connectivities would be interesting [16, 9, 21]. The long connectivity of domains may also help the production of nanoporous materials by dealloying of the less noble component [10, 19, 4]. One of the technical difficulties of dealloying processes is to warrant that the remaining component forms very long connected clusters, but the present models suggests that such clusters are already present in the precursor films. Indeed, recent works on dealloying of sputter-deposited NiAl films [37] and AgAu films [26] suggest that the connectivity of the final porous materials (Ni and Au films, respectively) evolved from the connectivity of their components in the precursors.

At high temperatures, we showed an enhanced separation of domains, which parallels the observations of previous models [2, 42, 52, 40]. The increase in the width of the finite, nanosized domains is usually accompanied by a loss of the long range connectivity, with possible formation of gaps between domains of different species. The vertical orientation of the domains may also be impaired because the large surface mobility facilitates their lateral propagation during the formation of each atomic layer. Thus, the production of films with long connected clusters of the same species requires a careful control of temperature and deposition flux, which have to be set according to the energetics of both species.

We also observe that local surface fluctuations depend on the model parameters in a similar way of films with a single species. The main parameter controlling those fluctuations is the probability of adatom hops across

steps: as that rate increases, the surface becomes locally smoother. This smoothening is also obtained with the increase of the terrace diffusion coefficients. Thus, the local smoothening is generally a consequence of the increase of temperature or of the decrease of the deposition flux. However, at high temperatures, the value of the roughness W measured in the whole surface may be large because there are large height differences in the gaps between domains, although the top surfaces of individual domains are smooth.

We also investigated some cases in which the terrace diffusion coefficients of the two species differ by two orders of magnitude. The scaling of domain width with the model parameters is less accurate; rough estimates of those widths can be obtained using geometric averages of diffusion-to-deposition ratios (which are obtained from averages of the terrace diffusion coefficients of the two species), of probabilities of detachment from island borders, and of probabilities of hops across terrace steps. However, the species with the largest mobility determines the maximal temperature in which long connected domains can be obtained.

Note that the increase of a characteristic domain size with the increase of the temperature or with the decrease of the deposition rate was already observed in some previous models on deposition of binary alloy films [2, 27, 33, 24, 42, 25]. However, those models did not present the domain morphology described here, in which the different sizes that characterize a single domain may range from a few nanometers (the widths) to hundreds of nanometers or micrometers (the connected lengths in longitudinal directions). Thus, despite the simple features of our model, the results presented here may be useful to search for suitable conditions for producing two-component thin films with such nontrivial morphology.

5. Conclusion

We analyzed results of kinetic Monte Carlo simulations of deposition of thin films with two components, A and B, in conditions that favor domain formation: energy barriers for adatom diffusion are larger (smaller) when represent the interactions of adatoms of the same (different) species. The film morphology is determined in terms of the ratios between terrace diffusivity and atomic flux, of the probabilities of detachment from lateral neighbors, and of probabilities of crossing step barriers.

For low and intermediate temperatures, we observe the formation of narrow domains that meander in the layers parallel to the substrate. Their

widths are small (up to ~ 30 lattice constants), but they are connected through very long distances along the substrate directions. Scaling relations for the domain widths were obtained. Using tabulated values of the energy barriers in single species film deposition, those relations may be used to predict the orders of magnitude of domains in alloy films. At high temperatures, the domains are thicker, but their long range connectivity is lost. In cases of significantly different A-A and B-B interactions, the species with the largest terrace mobility is the one that constrains the temperature range in which the long domains are found.

Acknowledgements

FDAAR acknowledges support from the Brazilian agencies CNPq (grant number 305391/2018-6), CAPES (project number 88881.068506/2014-01), and FAPERJ (project numbers E-26/110.129/2013 and E-26/202.881/2018). TBTT acknowledges support from CAPES (grant number PNP20130933 - 31003010002P7).

Conflict of interest

The authors declared that there is no conflict of interest.

References

- [1] C. D. Adams, M. Atzmon, Y-T. Cheng, and D. J. Srolovitz. Phase separation during co-deposition of Al-Ge thin films. Journal of Materials Research, 7(3):653–666, 1992. doi: 10.1557/JMR.1992.0653.
- [2] C. D. Adams, D. J. Srolovitz, and M. Atzmon. Monte Carlo simulation of phase separation during thin-film codeposition. J. Appl. Phys., 74: 1707, 1993. doi: 10.1063/1.354825.
- [3] K. Ankit, B. Derby, R. Raghavan, A. Misra, and M. J. Demkowicz. 3-D phase-field simulations of self-organized composite morphologies in physical vapor deposited phase-separating binary alloys. J. Appl. Phys., 126:075306, 2019. doi: 10.1063/1.5110410.

- [4] M. A. Atwater, L. N. Guevara, K. A. Darling, and M. A. Tschopp. Solid state porous metal production: A review of the capabilities, characteristics, and challenges. Advanced Engineering Materials, 20:1700766, 2018. doi: 10.1002/adem.201700766.
- [5] R. Banerjee, J. Novák, C. Frank, C. Lorch, A. Hinderhofer, A. Gerlach, and F. Schreiber. Evidence for kinetically limited thickness dependent phase separation in organic thin film blends. Phys. Rev. Lett., 110:185506, May 2013. doi: 10.1103/PhysRevLett.110.185506. URL <https://link.aps.org/doi/10.1103/PhysRevLett.110.185506>.
- [6] A. Chame and F. D. A. Aarão Reis. Scaling of local interface width of statistical growth models. Surface Science, 553(1):145 – 154, 2004. ISSN 0039-6028. doi: <https://doi.org/10.1016/j.susc.2004.01.048>.
- [7] S. Clarke and D. D. Vvedensky. Growth kinetics and step density in reflection high-energy electron diffraction during molecular-beam epitaxy. J. Appl. Phys., 63:2272, 1988. doi: 10.1063/1.341041.
- [8] T. A. de Assis and F. D. A. Aarão Reis. Dynamic scaling and temperature effects in thin film roughening. J. Stat. Mech.: Theory and Experiment, 2015(6):P06023, 2015.
- [9] B. Derby, Y. Cui, J. K. Baldwin, and A. Misra. Effects of substrate temperature and deposition rate on the phase separated morphology of co-sputtered, Cu-Mo thin films. Thin Solid Films, 647:50–56, 2018.
- [10] Y. Ding and J. Erlebacher. Nanoporous metals with controlled multimodal pore size distribution. Journal of the American Chemical Society, 125(26):7772–7773, Jul 2003. ISSN 0002-7863. doi: 10.1021/ja035318g. URL <https://doi.org/10.1021/ja035318g>.
- [11] B. Drossel and M. Kardar. Model for growth of binary alloys with fast surface equilibration. Phys. Rev. E, 55:5026–5032, May 1997. doi: 10.1103/PhysRevE.55.5026. URL <https://link.aps.org/doi/10.1103/PhysRevE.55.5026>.
- [12] F. Dumont, F. Picaud, C. Ramseyer, and C. Girardet. Conditions for organized nanoring growth using kinetic Monte Carlo simulations. Phys. Rev. B, 77:153404, Apr 2008. doi: 10.1103/PhysRevB.77.153404. URL <https://link.aps.org/doi/10.1103/PhysRevB.77.153404>.

- [13] M. Einax, S. Ziehm, W. Dieterich, and P. Maass. Scaling of island densities in submonolayer growth of binary alloys. Phys. Rev. Lett., 99: 016106, Jul 2007. doi: 10.1103/PhysRevLett.99.016106. URL <https://link.aps.org/doi/10.1103/PhysRevLett.99.016106>.
- [14] M. Einax, W. Dieterich, and P. Maass. Binding energies between unlike atoms determined from island densities. J. Appl. Phys., 105:054312, 2009. doi: 10.1063/1.3086315.
- [15] M. Einax, W. Dieterich, and P. Maass. Colloquium: Cluster growth on surfaces: Densities, size distributions, and morphologies. Rev. Mod. Phys., 85:921–939, Jul 2013. doi: 10.1103/RevModPhys.85.921.
- [16] V. Elofsson, G. A. Almyras, B. Lü, R. D. Boyd, and K. Sarakinos. Atomic arrangement in immiscible Ag-Cu alloys synthesized far-from-equilibrium. Acta Materialia, 110:114 – 121, 2016. ISSN 1359-6454. doi: 10.1016/j.actamat.2016.03.023. URL <http://www.sciencedirect.com/science/article/pii/S1359645416301768>.
- [17] V. Elofsson, G. A. Almyras, B. Lü, M. Garbrecht, R. D. Boyd, and K. Sarakinos. Structure formation in Ag-X (X = Au, Cu) alloys synthesized far-from-equilibrium. J. Appl. Phys., 123:165301, 2018. doi: 10.1063/1.5018907.
- [18] J. W. Evans, P. A. Thiel, and M. C. Bartelt. Morphological evolution during epitaxial thin film growth: Formation of 2D islands and 3D mounds. Surface Science Reports, 61(1):1 – 128, 2006. ISSN 0167-5729. doi: <https://doi.org/10.1016/j.surfrep.2005.08.004>.
- [19] T. Fujita. Hierarchical nanoporous metals as a path toward the ultimate three-dimensional functionality. Science and Technology of Advanced Materials, 18(1):724–740, 2017. doi: 10.1080/14686996.2017.1377047. URL <https://doi.org/10.1080/14686996.2017.1377047>.
- [20] K. Fukutani, Y. Ishida, K. Tanji, and T. Den. Nanowire array fabricated by Al-Ge phase separation. Thin Solid Films, 515(11):4629 – 4635, 2007. ISSN 0040-6090. doi: 10.1016/j.tsf.2006.11.192. URL <http://www.sciencedirect.com/science/article/pii/S0040609006017147>.
- [21] N. Ghafoor, I. Petrov, D. Holec, G. Greczynski, J. Palisaitis, P. O. A. Persson, L. Hultman, and J. Birch. Self-structuring in $Zr_{1-x}Al_xN$ films

- as a function of composition and growth temperature. Scientific Reports, 8(1):16327, 2018. ISSN 2045-2322. doi: 10.1038/s41598-018-34279-w. URL <https://doi.org/10.1038/s41598-018-34279-w>.
- [22] Y. Han, D. Jing, B. Ünal, P. A. Thiel, and J. W. Evans. Far-from-equilibrium film growth on alloy surfaces: Ni and Al on NiAl(110). Phys. Rev. B, 84:113414, Sep 2011. doi: 10.1103/PhysRevB.84.113414. URL <https://link.aps.org/doi/10.1103/PhysRevB.84.113414>.
- [23] Y. Han, D.-J. Liu, and J. W. Evans. Real-time ab initio KMC simulation of the self-assembly and sintering of bimetallic epitaxial nanoclusters: Au + Ag on Ag(100). Nano Letters, 14(8):4646–4652, Aug 2014. ISSN 1530-6984. doi: 10.1021/nl5017128. URL <https://doi.org/10.1021/nl5017128>.
- [24] J. H. He, C. A. Carosella, G. K. Hubler, S. B. Qadri, and J. A. Sprague. Kinetic Monte Carlo simulations of nanoscale compositional patterning during film growth of phase-separated systems. Phys. Rev. B, 73:235406, Jun 2006. doi: 10.1103/PhysRevB.73.235406. URL <https://link.aps.org/doi/10.1103/PhysRevB.73.235406>.
- [25] M. Hennes, V. Schuler, X. Weng, J. Buchwald, D. Demaille, Y. Zheng, and F. Vidal. Growth of vertically aligned nanowires in metal-oxide nanocomposites: kinetic Monte-Carlo modeling versus experiments. Nanoscale, 10:7666–7675, 2018. doi: 10.1039/C7NR08974K. URL <http://dx.doi.org/10.1039/C7NR08974K>.
- [26] L.-W. Hu, X. Liu, G.-M. Le, J.-F. Li, F.-S. Qu, S.-Y. Lu, and L. Qi. Morphology evolution and SERS activity of the nanoporous Au prepared by dealloying sputtered Au-Ag film. Physica B: Condensed Matter, 558:49 – 53, 2019. ISSN 0921-4526. doi: 10.1016/j.physb.2019.01.019. URL <http://www.sciencedirect.com/science/article/pii/S0921452619300195>.
- [27] G. Kairaitis and A. Galdikas. Phase separation during thin film deposition. Computational Materials Science, 91:68 – 74, 2014. ISSN 0927-0256. doi: 10.1016/j.commatsci.2014.04.034. URL <http://www.sciencedirect.com/science/article/pii/S0927025614002766>.

- [28] G. Kairaitis, A. Grigaliūnas, A. Baginskas, and A. Galdikas. Kinetic modeling of phase separation and surface segregation in growing a-C:Ni thin films. Surface and Coatings Technology, 352:120 – 127, 2018. ISSN 0257-8972. doi: 10.1016/j.surfcoat.2018.08.012. URL <http://www.sciencedirect.com/science/article/pii/S025789721830817X>.
- [29] M. Kotrla, J. Krug, and P. Šmilauer. Submonolayer epitaxy with impurities: Kinetic Monte Carlo simulations and rate-equation analysis. Phys. Rev. B, 62:2889–2898, Jul 2000. doi: 10.1103/PhysRevB.62.2889. URL <https://link.aps.org/doi/10.1103/PhysRevB.62.2889>.
- [30] T. F. Kuech, S. E. Babcock, and L. Mawst. Growth far from equilibrium: Examples from III-V semiconductors. Appl. Phys. Rev., 3:040801, 2016. doi: 10.1063/1.4944801.
- [31] P.-M. Lam, R. Tashakkori, and K. Yu. Effect of monomer evaporation in the Clark-Vvedensky model of submonolayer growth. Phys. Rev. B, 56:4893–4899, Aug 1997. doi: 10.1103/PhysRevB.56.4893. URL <https://link.aps.org/doi/10.1103/PhysRevB.56.4893>.
- [32] F. F. Leal, S. C. Ferreira, and S. O. Ferreira. Modelling of epitaxial film growth with an Ehrlich-Schwöebel barrier dependent on the step height. Journal of Physics: Condensed Matter, 23(29):292201, 2011.
- [33] F. Léonard, M. Laradji, and R. C. Desai. Molecular beam epitaxy in the presence of phase separation. Phys. Rev. B, 55:1887–1894, Jan 1997. doi: 10.1103/PhysRevB.55.1887. URL <https://link.aps.org/doi/10.1103/PhysRevB.55.1887>.
- [34] C. Lorch, J. Novák, R. Banerjee, S. Weimer, J. Dieterle, C. Frank, A. Hinderhofer, A. Gerlach, F. Carla, and F. Schreiber. Influence of C_{60} co-deposition on the growth kinetics of diindenoperylene-from rapid roughening to layer-by-layer growth in blended organic films. J. Chem. Phys., 146:052807, 2017. doi: 10.1063/1.4966583.
- [35] Xiao Lu, Boya Lai, Vignesh Sundar, Jian-Gang Zhu, David E. Laughlin, and Jingxi Zhu. Understanding the nanostructure formation of the templated two- phase film growth via hybrid modeling. Cryst. Growth Des., 17:1016–1027, 2017.

- [36] Y. Lu, C. Wang, Y. Gao, R. Shi, X. Liu, and Y. Wang. Microstructure map for self-organized phase separation during film deposition. *Phys. Rev. Lett.*, 109:086101, Aug 2012. doi: 10.1103/PhysRevLett.109.086101. URL <https://link.aps.org/doi/10.1103/PhysRevLett.109.086101>.
- [37] B. Luo, T. Wu, L. Zhang, F. Diao, Y. Zhang, L. Ci, J. Ulstrup, J. Zhang, and P. Si. Monometallic nanoporous nickel with high catalytic performance towards hydrazine electro-conversion and its DFT calculations. *Electrochimica Acta*, 317:449 – 458, 2019. ISSN 0013-4686. doi: 10.1016/j.electacta.2019.05.123. URL <http://www.sciencedirect.com/science/article/pii/S0013468619310564>.
- [38] Satya N. Majumdar and Alan J. Bray. Spatial persistence of fluctuating interfaces. *Phys. Rev. Lett.*, 86:3700–3703, 2001. doi: 10.1103/PhysRevLett.86.3700.
- [39] T. Michely and J. Krug. *Islands, Mounds, and Atoms*. Springer, 2003.
- [40] M. Mińkowski, M. A. Załuska-Kotur, Ł. A. Turski, and G. Karczewski. Monte Carlo simulations of morphological transitions in PbTe/CdTe immiscible material systems. *J. Appl. Phys.*, 120:124305, 2016. doi: 10.1063/1.4962974.
- [41] M. Mińkowski, M. A. Załuska-Kotur, S. Kret, S. Chusnutdinow, S. Schreyeck, K. Brunner, L. W. Molenkamp, and G. Karczewski. Self-organization process in crystalline PbTe/CdTe multilayer structures: Experiment and Monte Carlo simulations. *Journal of Alloys and Compounds*, 747:809 – 814, 2018. ISSN 0925-8388. doi: 10.1016/j.jallcom.2018.03.079. URL <http://www.sciencedirect.com/science/article/pii/S092583881830940X>.
- [42] I. Mouton, E. Talbot, C. Pareige, R. Lardé, and D. Blavette. The early stage of formation of self-organized nanocolumns in thin films: Monte Carlo simulations versus atomic-scale observations in Ge-Mn. *J. Appl. Phys.*, 115:053515, 2014. doi: 10.1063/1.4864271.
- [43] T. J. Oliveira and F. D. A. Aarão Reis. Scaling in reversible sub-monolayer deposition. *Phys. Rev. B*, 87:235430, Jun 2013. doi: 10.1103/PhysRevB.87.235430.

- [44] G. V. Rodriguez and J. M. Millunchick. Predictive modeling of low solubility semiconductor alloys. J. Appl. Phys., 120:125310, 2016. doi: 10.1063/1.4962849.
- [45] R. L. Schwöebel. Step motion on crystal surfaces II. J. Appl. Phys., 40: 614, 1969.
- [46] D. Stauffer and A. Aharony. Introduction to percolation theory. Taylor & Francis, London, 2nd edition, 1992. doi: 10.1201/9781315274386.
- [47] C. R. Tait, L. Yan, and J. M. Millunchick. Spontaneous nanostructure formation in GaAsBi alloys. Journal of Crystal Growth, 493: 20 – 24, 2018. ISSN 0022-0248. doi: 10.1016/j.jcrysgro.2018.04.026. URL <http://www.sciencedirect.com/science/article/pii/S0022024818301982>.
- [48] X. Tao, Y. Shim, and D. P. Landau. Monte Carlo simulation of film growth in a phase separating binary alloy model. Physica A: Statistical Mechanics and its Applications, 387(11):2495 – 2503, 2008. ISSN 0378-4371. doi: 10.1016/j.physa.2008.01.014. URL <http://www.sciencedirect.com/science/article/pii/S0378437108000307>.
- [49] A. Thøgersen, I. J. T. Jensen, M. Stange, T. Kjeldstad, D. Martinez-Martinez, O. M. Løvvik, A. G. Ulyashin, and S. Diplas. Formation of nanoporous Si upon self-organized growth of Al and Si nanostructures. Nanotechnology, 29(31):315602, may 2018. doi: 10.1088/1361-6528/aac36a. URL <https://doi.org/10.1088/1361-6528/aac36a>.
- [50] Y. Tian, P. Mukherjee, T. V. Jayaraman, Z. Xu, Y. Yu, L. Tan, D. J. Sellmyer, and J. E. Shield. Ultrahigh-density sub-10 nm nanowire array formation via surface-controlled phase separation. Nano Lett., 14(8): 4328–4333, June 2014. doi: 10.1021/nl501128c.
- [51] T. B. T. To, V. B. de Sousa, and F. D. A. Aarão Reis. Thin film growth models with long surface diffusion lengths. Physica A: Statistical Mechanics and its Applications, 511:240 – 250, 2018. ISSN 0378-4371. doi: 10.1016/j.physa.2018.07.024. URL <http://www.sciencedirect.com/science/article/pii/S0378437118308884>.
- [52] Y. Zhu and X. Pan. Kinetic Monte Carlo simulation of 3-D growth of NiTi alloy thin films. Applied Surface Science, 321:24 – 29, 2014.

ISSN 0169-4332. doi: 10.1016/j.apsusc.2014.09.115. URL <http://www.sciencedirect.com/science/article/pii/S0169433214021060>.